Energy & Environmental Science

Cite this: *Energy Environ. Sci.*, 2012, **5**, 8708

www.rsc.org/ees

PAPER

Phase and shape controlled VO_2 nanostructures by antimony doping†

Yanfeng Gao,*[a] Chuanxiang Cao,[a] Lei Dai,[ab] Hongjie Luo,[c] Minoru Kanehira,[a] Yong Ding[d] and Zhong Lin Wang*[d]

Received 21st May 2012, Accepted 10th July 2012
DOI: 10.1039/c2ee22290f

Quasi-spherical VO_2 nanoparticles with uniform size and high crystallinity are ideal functional materials for applications in field-effect transistors, smart window coatings and switches. However, the synthesis of these VO_2 nanoparticles has long been a challenge. This article presents a novel doping strategy for the simultaneous control of the size, morphology and polymorphology of VO_2 nanoparticles. Doping can induce the change in crystal structure and exhibits a significant promoting effect on the formation of doped monoclinic VO_2 (VO_2 (M)). Specifically, by antimony (Sb^{3+}) doping, hexagonal-shaped, well crystalline monoclinic VO_2 nanoparticles with tunable sizes (8–30 nm) and controllable polymorphs were synthesized *via* a one-pot, hydrothermal method. Sb^{3+} dopants, which are larger in radius and lower in valence than V^{4+} ions, can introduce extra oxygen vacancies during the nucleation and growth of VO_2 nanoparticles. These positively charged nuclei may suppress the adsorption of VO^{2+} aqua ions, and therefore inhibit the growth of the VO_2 (M) nanoparticles. Comparably, Sb^{5+} dopants that possess higher valence counts than V^{4+} ions can induce the growth of VO_2 (M) particles to 200–300 nm width and above 500 nm length. The Sb^{3+}-doped VO_2 (M) nanoparticles exhibit excellent properties in metal–semiconductor transformation at transition temperatures ranging from 55–68 °C. Films obtained by casting these nanoparticles show excellent optical properties (both visible transmittance and infrared regulation), compared with those prepared from gas phases, such as sputtering. This synthetic strategy that involves the doping of an element with a different valence count than the matrix cation may be useful for controlling the solution growth of some technologically significant nanomaterials. In addition, the formation mechanism of solid and crystalline transformation was also studied by designing a specific reaction autoclave.

[a]*State Key Laboratory of High Performance Ceramics and Superfine Microstructure, Shanghai Institute of Ceramics (SIC), Chinese Academy of Sciences (CAS), Dingxi 1295, Changning, Shanghai, 200050, China. E-mail: yfgao@mail.sic.ac.cn; Fax: +86-21-5241-5270; Tel: +86-21-5241-5270*
[b]*Graduate University of Chinese Academy of Sciences, Yuquanlu 19, Beijing, 100049, China*
[c]*Shanghai Institute of Ceramics (SIC), Chinese Academy of Sciences (CAS), Dingxi 1295, Changning, Shanghai, 200050, China*
[d]*School of Materials Science and Engineering, Georgia Institute of Technology, 771 Ferst Dr. N.W., Atlanta, GA 30332, USA. E-mail: zhong.wang@mse.gatech.edu; Tel: +1-404-894-8008*
† Electronic supplementary information (ESI) available. See DOI: 10.1039/c2ee22290f

Broader context

Smart windows refer to a glass window that enables users to intelligently control the amount of light and heat passing through, usually by an external stimulus such as electrical field (electrochromic), temperature (thermochromic), ultraviolet irradiation (photochromic) and reductive or oxidizing gases (gasochromic). VO_2 in the monoclinic or rutile phase possesses a character that is called Mott phase transition, and is a crucial thermochromic material that can absorb ultra-violet light and change infrared transmittance by response to an environmental temperature change. There are usually two methods for the preparation of VO_2-based smart windows. The first is based on gas-phase reactions such as sputtering and chemical vapor deposition, and the second is solution-related methods such as polymer-assisted deposition (see a review article: *Nano Energy*, 2012, **1**, 221–246). Nanoparticles with controllable size, crystalline phase and morphology offer an alternative means for the preparation of films by solution methods, especially on temperature-sensitive, flexible polymer surfaces.

Introduction

Doping, which involves the intentional incorporation of atoms or ions of suitable elements into host lattices, is widely applied in various technological processes for the controlled manipulation of the electronic, magnetic and emission properties of nanocrystals.[1–5] Recent studies have demonstrated that doping also provides a fundamental approach to modify the growth behaviors of functional nanomaterials to achieve control over the crystallographic phase.[6–9] Luwang *et al.* reported the phase transformation from a tetragonal to a hexagonal structure, which was caused by increasing cerium (Ce^{3+}) concentrations in YPO_4:Eu.[7] Liu and co-workers demonstrated that lanthanide doping has an ability to tune the size and phase of $NaYF_4$ nanocrystals.[8] Furthermore, doping also has the ability to control the size[6,9–12] and morphology[5,8,13–16] of nanocrystals using various mechanisms, such as competitive nucleation[8] and the dipole polarizability of the dopant ion.[6–9] Therefore, understanding the underlying mechanism and extending the preparation method for functional nanoparticles with precise control of their sizes,[17] crystalline phases[18] and morphologies would enable their use in a number of important applications. However, most of the research in this area is focused on synthesizing upconversion-luminescent nanocrystals; there are currently very few studies that involve other functional nanomaterials except luminescent nanocrystals. In this article, we report a novel doping strategy for the simultaneous control of the size, morphology and polymorphology of vanadium dioxide (VO_2) nanoparticles. Moreover, the VO_2 nanoparticle-derived films exhibit excellent optical properties and suggest promising application to energy-efficient smart windows.

In recent years, monoclinic vanadium dioxide (VO_2 (M)) has been the subject of an intensive research effort due to its potential applications in the design of smart window coatings[19] and in other advanced devices, such as field-effect transistors,[20] sensors,[21] and switches.[20] Most of these applications are based on a fully reversible, temperature-dependent metal–semiconductor transition (MST) that occurs in a pure, undoped bulk material at approximately 68 °C.[22] This first-order structural transition from the insulating VO_2 (M) form to the metallic rutile form (VO_2 (R)) may cause a drastic change in the electrical and optical properties of the materials.[23] However, this transition possesses a high crystallographic selection and also relies on the polymorphism, crystallinity and size of the VO_2 crystallites. Thus far, more than ten types of VO_2 crystalline phases have been reported. The most familiar ones are the following: tetragonal rutile-type, VO_2 (R) (*P*4/*mmm*); monoclinic rutile-type, VO_2 (M) (*P*21/*c*); low-temperature phase (LTP) tetragonal VO_2 (A) (*P*4/*ncc*); high-temperature phase (HTP) tetragonal VO_2 (A) (*I*4/*m*) and monoclinic VO_2 (B) (*C*2/*m*). The crystallographic structures of the above five VO_2 polymorphs are based on an oxygen *bcc* lattice, in which vanadium ions sit in the octahedral sites and the oxygen octahedra are more or less regular. Among these crystalline polymorphs, only VO_2 (M) and VO_2 (R) demonstrate the MST phase-transition character mentioned above. VO_2 (M) is usually synthesized by transforming VO_2 (B/A) at elevated temperatures, and it is usually very hard to produce a pure phase in one step. We have previously synthesized pure-phase VO_2 (M) particles *via* a one-step hydrothermal reaction.[24] This direct solution synthesis method has been proven to be powerful, and could be applied for the synthesis of pure VO_2 (M) nanoparticles, which is a thermodynamically stable phase, in large quantities. However, the VO_2 (M) particles show snowflake aggregation with preferential orientation growth along the [110] direction, limiting their dispersion, transparency and overall application to smart windows. The monoclinic VO_2 (M) has a preferential orientation along the [110] direction and is prone to grow to one-dimensional nanostructures, such as nanowires, nanorods and nanobelts.[24–28] Son and co-workers[29] synthesized a mixture containing hexagon-shaped VO_2 (M) nanocrystals and VO_2 (B) nanowires, but the work shows that it is difficult to control the crystallographic phase, size and shape of VO_2 nanoparticles at the same time.

Quasi-spherical VO_2 (M) nanoparticles with uniform sizes and high crystallinity are ideal for superior performance because these particles are a fundamental component to prepare stable dispersions, which are a requisite to achieve good visible transmittance and the regulation ability of infrared light. However, the formation of spherical VO_2 particles is a challenge because it requires the induced growth of low-energy surfaces or the suppressed growth of energetically unfavorable high-index faces.

Doping is an important technique for regulating the transition temperature of VO_2 (M). However, we report a novel doping strategy for the simultaneous control of the size, morphology and polymorphology of these materials. Hexagonal-shaped, well crystalline, antimony (Sb^{3+})-doped VO_2 (M) nanoparticles with tunable sizes were synthesized *via* a one-pot hydrothermal method. The formation mechanism was also studied by temperature-resolved observation of products using a home-made autoclave. These nanoparticles are dispersible in an aqueous solvent and exhibit a strong MST character. Films obtained by casting these nanoparticles demonstrate excellent optical properties.

Experiments and methods

All reagents were bought from Sinopharm Chemical Reagent Co., Ltd., and used without further purification. Vanadium pentoxide (V_2O_5, analytically pure) and diamide hydrochloride ($N_2H_4 \cdot HCl$, analytically pure) were employed as starting materials to prepare a VO^{2+} solution. Concentrated HCl (6 mL, 38%) solution and a solution containing 1 g of $N_2H_4 \cdot HCl$ were added into an aqueous suspension (20 mL) containing 3.5 g of V_2O_5. The solution was treated with a small amount of V_2O_5 or $N_2H_4 \cdot HCl$ until it contained no VO_2^+ and V^{3+} and was then filtered to form a clear VO^{2+} solution (pH ≈ 1). To this solution, calculated amounts of the dopant Sb_2O_3 (analytically pure) were added. The solution was stirred for 10 min and then transferred to a 100 mL autoclave with a Teflon liner. The hydrothermal reaction was carried out at 200–260 °C for defined times. The final black product was separated by filtration or centrifugation, and washed with water and ethanol. The final doping ratios were confirmed by inductively coupled plasma (ICP, Thermoelectron Corporation, IRIS Intrepid). An undoped sample was synthesized following similar procedures. Experimentally, 3% Sb^{5+}-doped VO_2 nanocrystals, with a pure monoclinic phase, were prepared using the same method and Sb_2O_5 (analytically pure) as raw material. The oxidation states of the Sb were detected by

XPS. Bi_2O_3 and Ti_2O_3 (analytically pure) were used as raw materials for Bi^{3+} and Ti^{3+} doping. The film for the measurement of the optical property was prepared by the casting method. In detail, the VO_2 nanoparticles were mixed with a liquid precursor of waterborne polyurethane. 1 mL of dispersion liquid (waterborne polyurethane) with a 0.2% solid content was dripped on a 200 mm × 200 mm poly(ethylene terephthalate) (PET) substrate by the casting method, and then dried in an oven at 90 °C for 60 minutes. A homogeneous flexible film was obtained by this method.

For the study of the formation mechanism, a trace amount of product was collected at different reaction temperatures by using a home-made hydrothermal reactor that permits us to extract the products under high temperatures and pressures. The home-made hydrothermal reactor possesses a metal pipe introduced to the reactor from the bottom, and the other side of the pipe connecting with a valve and a cooling tower. When opening the valve, the high temperature solution can quickly pass through the cooling tower, and the sample was quickly cooled down to room temperature (from 260 to 80 °C in less than 2 s) to keep the product unchanged.

Characterization

The morphologies and sizes of the resulting products were characterized by transmission electron microscopy (TEM, JEM2010 and JEM 4000EX, JEOL, Tokyo, Japan). The crystal structures of the resulting products were characterized using a Japan Rigaku D/max 2550V X-ray diffractometer (Cu Kα, λ = 0.15406 nm). Differential scanning calorimetry (DSC, DSC204F1, NETZSCH) experiments were performed in nitrogen flow in the temperature range of −50 to 100 °C with a heating rate of 5 °C min^{-1}. The sample transmittance spectra at normal incidence from 240 to 2600 nm were measured using a Hitachi U-4100 spectrometer. The oxidation states of the Sb were detected by X-ray photoelectron spectroscopy (XPS, Kratos Axis Ultra DLD).

Results and discussion

Fig. 1a shows the X-ray diffraction (XRD) patterns of undoped and Sb^{3+}-doped VO_2 nanoparticles. Without Sb^{3+} doping, all peaks can be indexed to VO_2 (A). For the sample with an addition of 1% Sb^{3+}, VO_2 (A) is still a major phase. However, a small peak at 27.6° that corresponds to the (110) diffraction plane of VO_2 (M) is clearly observed, suggesting the formation of VO_2 (M) as a minor phase. As the additive amount of Sb^{3+} increased to 3% atom, VO_2 (M) became a main phase. Pure VO_2 (M) was obtained for the Sb^{3+} additive concentration of 5%, 15% and 40%. Additionally, no peaks for Sb_2O_3 or antimony trioxide were observed, suggesting the formation of a VO_2–Sb_2O_3 solid solution. The final chemical compositions were detected by inductively coupled plasma (ICP) (Table 1), which confirmed a success in doping of Sb^{3+} in VO_2, although the final doping amounts are a little lower than those added. Furthermore, in conducting thorough analyses of the XRD pattern, the widening of the VO_2 (M) peaks (011) is obviously observed, suggesting that the grain size decreases with doping concentration increasing. The (200) peak shows a significant migration to lower angles with

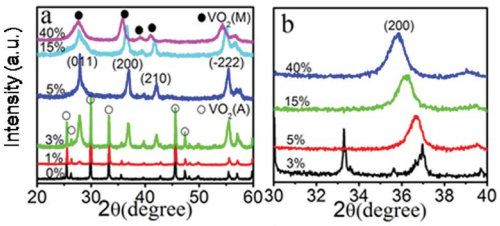

Fig. 1 (a) XRD patterns of the VO_2 powders with and without Sb^{3+} doping; (b) a magnified pattern of the (200) peak.

Table 1 The addition amount of Sb^{3+} and the corresponding molar ratio of Sb^{3+} in final products

Addition amount (atom%)	0.5%	1%	3%	5%	15%	40%
Final doping ratios (atom%)	0.48%	0.91%	2.68%	4.69%	13.60%	33.10%

increasing Sb^{3+} content (Fig. 1b), because the Sb^{3+} ion substituting the V^{4+} ion is larger. These results suggest that an appropriate amount of Sb^{3+} dopant can promote the phase transition from VO_2 (A) to VO_2 (M). The changes in the crystalline phase and morphology induced by doping can also be observed by transmission electron microscopy (TEM). Without doping Sb^{3+}, all of the particles show uniform rod shapes (Fig. 2a and b). A high-resolution TEM image recorded from the selected area of the tip of an individual rod (Fig. 2c) confirmed high crystallinity. A selected area electron diffraction (SAED) pattern is indexed to VO_2 (A) with a zone axis of [110] (Fig. 2d). A comparative study of the experimental (Fig. 2d) and simulation results (Fig. 2e and f) suggests that the VO_2 (A) is more likely to take the *P4/ncc* space group (a = 8.4403, c = 7.666, JCPDF card: 04-007-2429). The SAED patterns of the products also reveal the orientation of the VO_2 (A) rod with a side surface belonging to the {110} plane (Fig. 2d), which is in agreement with another SAED pattern (Fig. 2g) and a HRTEM image (Fig. 2i) from another side of the rod (Fig. 2h). All of the above analyses revealed that the VO_2 (A) nanorods grow with a preferential orientation along the [001] direction, which may be determined by a relative surface energy of the planes at various crystal faces. As the crystal structure of VO_2 (A) shown in Fig. 3a, the distance between the {110} planes (the dashed line in Fig. 3a) is longer than the others. It indicates that the (110) plane has a relatively low stacking rate and as a low-energy surface, the (110) plane favors to be exposed and grown along the [001] axis.

With 1% dopant, the number and the diameter of the rod-shaped particles in the product obviously decreased (Fig. 4a) compared with the undoped sample, so as that with 2% dopant (results not shown). However, when the Sb^{3+} addition content was increased to 3% atom, most of the particles were hexagon-shaped with a mean size of 30 nm (Fig. 4c and inset). The particle size decreased with increasing Sb^{3+} amounts; a mean diameter of 8 nm was observed for the sample with a 40% addition of Sb_2O_3 (Fig. 4c and inset). Remarkably, TEM observations provided evidence that the size of these small nanocrystals was gradually reduced and that the size distribution tended to be more homogeneous with increasing Sb^{3+} contents (Fig. 4a–c). Notably, to

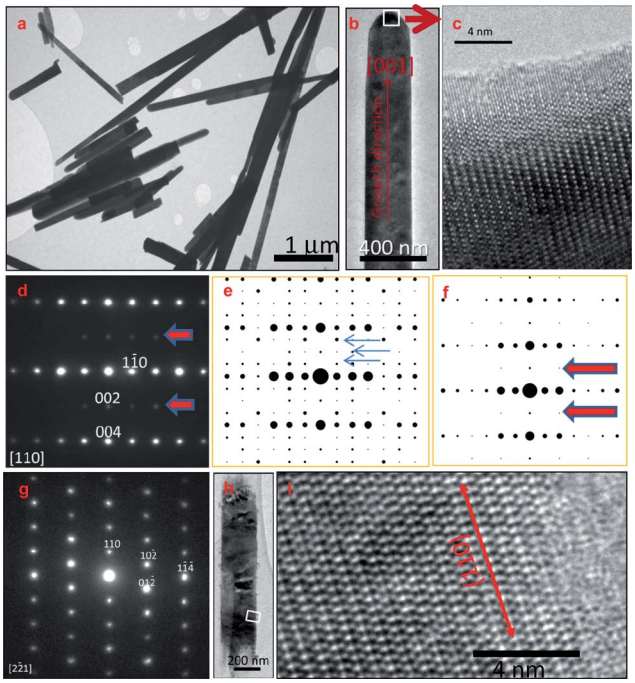

Fig. 2 (a) TEM images of the VO_2 powders prepared by the hydrothermal treatment at 260 °C for 12 h without addition of Sb^{3+}; (b) a magnified TEM image of a VO_2 (A) rod; (c) the corresponding SAED pattern of the VO_2 rod; (d) simulated diffraction [110] zone axis patterns for the space groups *P*42/*ncm* (138) and (e) *P*4/*ncc* (130); (g) another set of diffraction patterns of the VO_2 rod; (h) the square shows the spot for HRTEM observation; (i) HRTEM image of the spot shown in (h).

ensure the formation of pure VO_2 (M) nanocrystals, the highest Sb^{3+}-doping content was found to be 33.1% under the current synthetic conditions.

SAED patterns of rods in Fig. 4a were assigned to VO_2 (A), and meanwhile the appearance of small particles was also

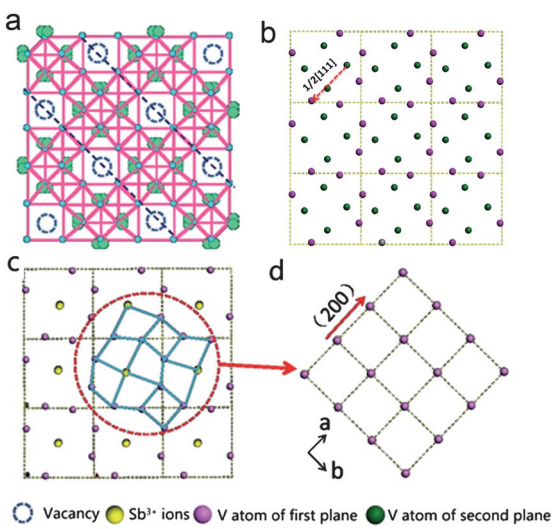

Fig. 3 (a) Projection of the crystallographic structures of VO_2 (A); (b) projection of the V atoms distribution of the HTP VO_2 (A) projected along the *c* axis; (c) the arrangement of V atoms in the first layer of the HTP VO_2 (A) and (d) VO_2 (R).

observable (Fig. 4a and an enlarged area of Fig. 4a (Fig. 4d)). This is clearer in another spot for the sample with 1% dopant (Fig. 4d′). These small particles could be assigned to VO_2 (M), which was confirmed by SAED analysis (Fig. 4d′, inset), and is in accordance with those with 3% and 40% dopants (Fig. 4e and f). HRTEM images clearly show that these particles are single crystals with high crystallinities. These data were in good agreement with the XRD results.

By carefully analyzing the XRD and TEM results, we can get two conclusions: one is that an appropriate amount of Sb^{3+} dopant can promote the phase transition from VO_2 (A) to VO_2 (M), and another is that increasing the Sb^{3+} doping amounts can decrease the particle size. In order to understand the mechanism of Sb^{3+} doping on promoting the phase transition from VO_2 (A) to VO_2 (M), we need to clarify the crystallographic characters of the involved polymorphs. Similar to the phase transition from VO_2 (M) to VO_2 (R), VO_2 (A) also occurs at a phase transition from the low-temperature phase (LTP) VO_2 (A) to the high-temperature phase (HTP) VO_2 (A) at about 162 °C.[30] In our experiment, because the reaction temperature of 260 °C is much higher than 162 °C, the as-prepared compounds should be the HTP VO_2 (A) and the VO_2 (R). Both the HTP VO_2 (A) and VO_2 (R) structures are based on the oxygen *bcc* lattice, in which vanadium atoms occupy part of the octahedral sites, solely the V atom distributions in the two polymorphous are different. Fig. 3a shows the lattice structure of the HTP VO_2 (A) projected along the *c* axis, and Fig. 3b only shows the V atom distributions of the HTP VO_2 (A) projected along the *c* axis. The arrangements of V atoms in the first (pink color) and second (green color) layers are the same; they just have a shift of 1/2[111] between them. It is the same case in polymorph VO_2 (R). In each layer, the arrangement of V atoms is not continuous; there are some free spaces, which could serve as the dopant location. Fig. 3b and c only show the cation distribution in the first layer in HTP VO_2 (A) and VO_2 (R), separately. If the dopant Sb^{3+} ions move to the biggest vacancy in the lattice of the VO_2 (A) structure (the dotted circles shown in Fig. 3a), the first V atom plane of the doped VO_2 (A) changes to a similar structure to the VO_2 (R), indicating that doping could induce the formation of the VO_2 (R) phase structure. The partial substitution of V^{4+} with Sb^{3+} ions causes the distortion of V atoms distribution because the diameter of Sb^{3+} is larger than that of V^{4+}. Because the Sb^{3+} ions were doped along the [200] direction, the shift of the (200) peak to lower angles was much larger than other peaks. Through the same mechanism, our previous works suggest that doping Mo^{6+} and W^{6+} ions has similar effects on the induction formation of the VO_2 (M) by the transformation from other polymorphs in a V_2O_5–oxalic acid system.[24]

To understand the mechanism of Sb^{3+} doping on decreasing the particle size, we designed a reactor to study the hydrothermal reactions. The sample with the addition of 3% Sb^{3+} is crucial to understand the effective mechanism of Sb^{3+} doping on the formation and growth processes of the VO_2 nanoparticles because this is a critical concentration of the transition from the VO_2 (A) rods to the VO_2 (M) nanoparticles. The temperature-resolved samples with 3% Sb^{3+} were collected at different reaction times using a particular hydrothermal reactor, which can decimate a small amount of reaction suspension during the hydrothermal process. The sample was fast cooled

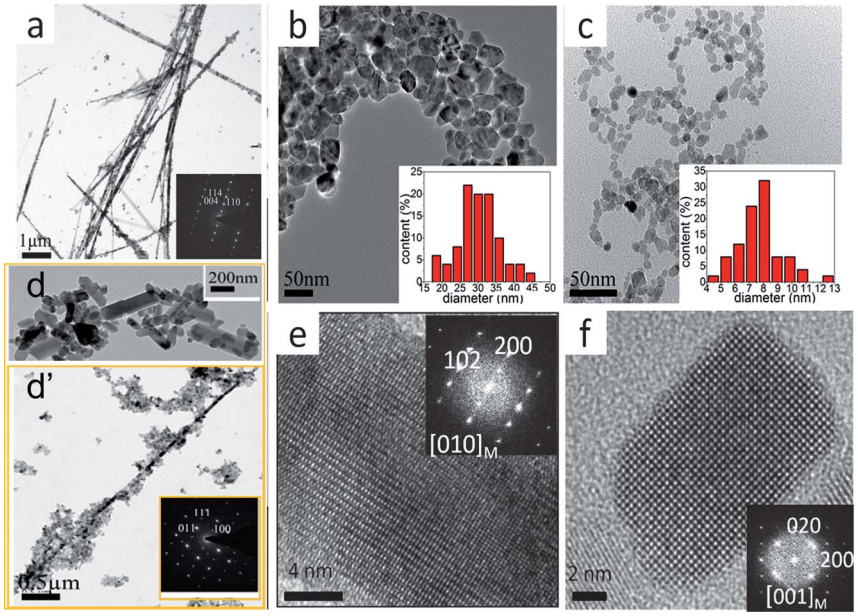

Fig. 4 TEM images of the VO_2 powders prepared by the hydrothermal treatment at 260 °C for 12 h with a Sb^{3+} addition of (a) 1%, (b) 3%, and (c) 40%. (d) A magnified TEM image of the hexagon-shaped VO_2 (M) particles represented in Fig. 3a. (d′) Another spot observed by TEM for VO_2 powders with a Sb^{3+} doping of 1% (inset shows SAED pattern of the hexagon-shaped VO_2 (M) particles shown in Fig. 3d). A HRTEM image (inset, the SAED pattern) of the VO_2 powders with a Sb^{3+} addition of (e) 3% and (f) 40%.

down to room temperature (from 260 to 50 °C in less than 2 s) to keep the sample unchanged. At the initial stage (under 200 °C), the vanadium source mainly existed in the form of VO^{2+} aqua ions (the precursor for the crystal growth of VO_2). When the temperature reached 210 °C, the VO^{2+} began to nucleate and formed a large number of rod-like VO_2 nuclei (Fig. 5a). The TEM results indicated that the nuclei were formed by a homogeneous nucleation mechanism because these rod-like particles are homogeneous in size. The diffraction rings observed by the SAED (the inset in Fig. 5a) revealed the poor crystallinity of the nuclei. As the temperature increased from 210 °C to 230 °C, some of the rod-like VO_2 nuclei began to grow and formed VO_2 rods (Fig. 5b). The selected area electron diffraction (SAED) pattern taken from an individual rod (the inset in Fig. 5b) was assigned to VO_2 (A). Moreover, there were no peaks for Sb (Fig. S1†) observed by energy dispersive X-ray spectroscopy (EDS), which indicates that the Sb elements were mainly in ion states in the solution at temperatures below 230 °C. When the temperature reached 250 °C, the product consisted of a large quantity of rods and a small amount of nanoparticles, as shown in Fig. 5c. The SAED taken from an individual rod (the inset in Fig. 5d) was indexed to VO_2 (A), while the diffraction rings (the inset in Fig. 5e) taken from the spherical nanoparticles was indexed to VO_2 (M). Careful analyses of the EDS (Fig. 5f) taken from rods and nanoparticles show that there is only a trace amount of Sb in the rods but about 5% in the nanoparticles, which is higher than that originally added. These findings suggest that the Sb^{3+} doping promoted the formation of VO_2 (M) nanoparticles from the rod-like VO_2 nuclei at about 240–250 °C. As the temperature was increased to 260 °C and/or the reaction time was prolonged, the VO_2 (A) rods transformed into VO_2 (M) nanoparticles most likely due to dissolution-recrystallization.

Below is a proposed mechanism that is responsible for the production of VO_2 nanoparticles with uneven shapes and sizes by the substitution of Sb^{3+} ions for V^{4+}. Without Sb^{3+} doping, VO_2 (A) nanorods grow with a preferential orientation along the [001] direction by the manner of oriented attachment. With Sb^{3+} doping, on one hand, the substitution of two ions of Sb^{3+} for V^{4+} in VO_2 requires an extra oxygen vacancy for charge compensation, and higher surface energy of nanoparticles favors oxygen vacancies to aggregate on their surfaces, which may induce transient electric dipoles with their positive poles outward. These transient electric dipoles hinder the diffusion of VO^{2+} as well as other charged nuclei to the grain surface, thus retarding the growth of VO_2 particles. On the other hand, the Sb^{3+}-doped VO_2 (A) shows a similar structure to VO_2 (R), promoting the formation of the VO_2 (R) phase. A schematic description of this mechanism for minimizing the size of VO_2 is presented in Fig. 6. At a low doping amount of Sb^{3+}, only limited numbers of VO_2 (R) seed crystals were produced, which means each seed crystal will get more reaction material from the dissolution-recrystallization of VO_2 (A) rods. Increasing the doping amounts of Sb^{3+} causes the formation of relatively more VO_2 (R) seed crystals and less VO_2 (A) rods, resulting in minimizing particle sizes.

The above discussion suggests that an extra repulsion force induced by dopant-resultant defects plays a significant role in the modification of particle sizes. This mechanism was confirmed by using other dopants in VO_2 systems. Using a high-valence ion dopant, such as Sb^{5+}, to substitute for V^{4+} sites in the VO_2 (M) lattice may induce negatively charged defects for the charge balance. The concentration of these defects on the grain surfaces causes an electric dipole that can accelerate the diffusion of VO^{2+} ions in solution to promote the grain growth. Experimentally, 3% Sb^{5+}-doped VO_2 nanocrystals, with a pure monoclinic phase, were successfully prepared using the same method (Fig. S2c†)

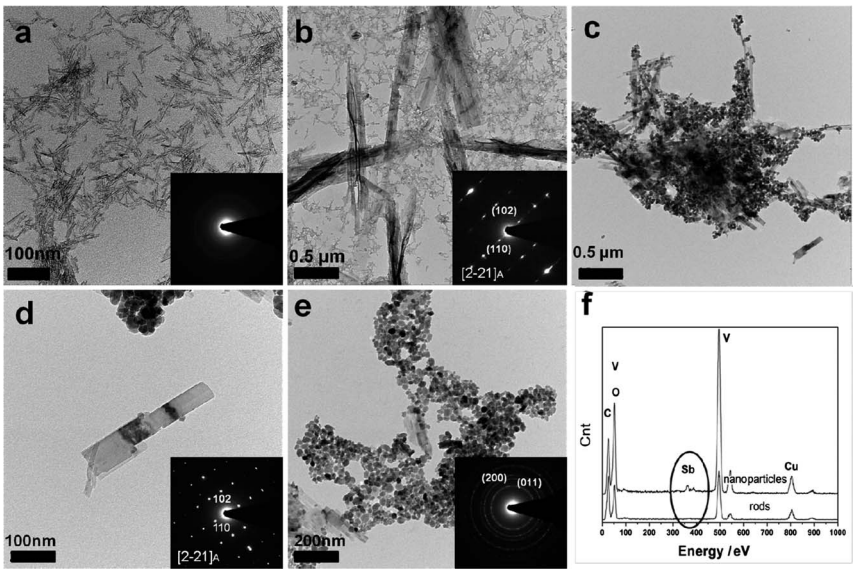

Fig. 5 TEM images (inset, the SAED pattern) of the VO_2 powders prepared by the hydrothermal treatment at (a) 210 °C, (b) 230 °C, and (c) 250 °C; (d) a magnified TEM image (inset, the SAED pattern) of the rods represented in (c); (e) a magnified TEM image (inset, the SAED pattern) of the nanoparticles represented in (c); (f) the EDS patterns taken from rods and nanoparticles prepared by the hydrothermal treatment at 250 °C.

and Sb_2O_5 as raw material. The oxidation states of the Sb were detected by XPS and the result was shown in Fig. S3†. However, the VO_2 (M) particles prepared with Sb^{5+} doping exhibited a relatively large size (200–300 nm in width and >500 nm in length) and were rod shaped. The impacts of Bi^{3+} and Ti^{3+} (using Bi_2O_3 and Ti_2O_3 as raw materials) doping on the growth of VO_2 nanocrystals under the analogous solution conditions were also studied to directly validate our proposed mechanism. Bi^{3+} and Ti^{3+} ions possess the same valence as Sb^{3+} and are speculated to induce similar effects in VO_2 crystal growth. As expected, both ion dopants benefit the formation of hexahedral VO_2 (M) nanocrystals with significantly smaller sizes (Fig. S2a and S2b†). The 3%-Bi^{3+}-doped VO_2 (M) particles exhibited an average particle size of approximately 50 nm. Contrastingly, 3%-Ti^{3+}-doped VO_2 (M) structures had an average particle size of approximately 40 nm. These results, in addition to others (Sb^{3+}, Mo^{6+}, Sb^{5+} and W^{6+} doping), entirely confirmed that doping is able to induce the transformation of VO_2 polymorphs.

The typical differential scanning calorimetry (DSC) curves of Sb^{3+}-doped VO_2 particles upon heating cycle are shown in Fig. 7a. The particles that were doped with 1%, 2% and 3% Sb^{3+} ions reported a similar MST temperature of 65 °C. However, the MST temperature decreased to approximately 62 °C for the particles prepared with the addition of 5% and 7% Sb^{3+} ions. Furthermore, due to an increase of the VO_2 (M) fractions in the products, the intensity of the DSC peaks increased with increasing doping amounts, and reached a maximum at an addition amount of 3%. However, the intensity of the DSC peaks decreased with increasing Sb^{3+} addition contents to above 5%. This phenomenon implies changed mechanisms of the effects of doping amounts on MST. The crystal structure changed with the metal-semiconductor transition. The low temperature,

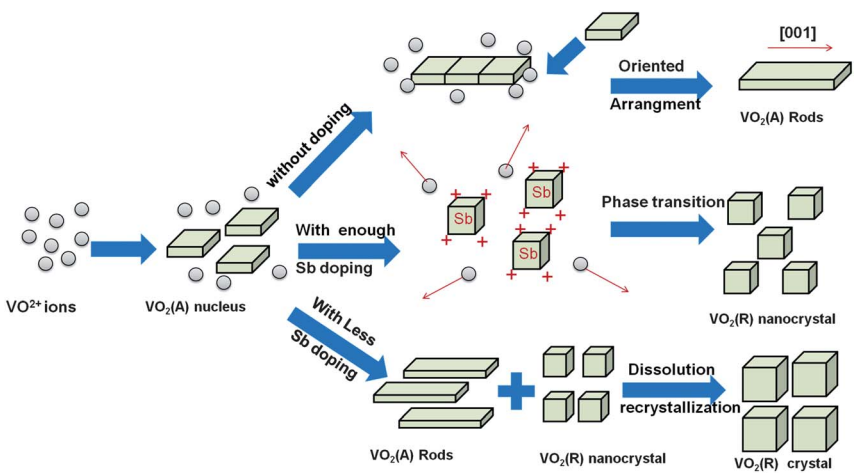

Fig. 6 A schematic illustration of the evolution of VO_2 nanoparticles.

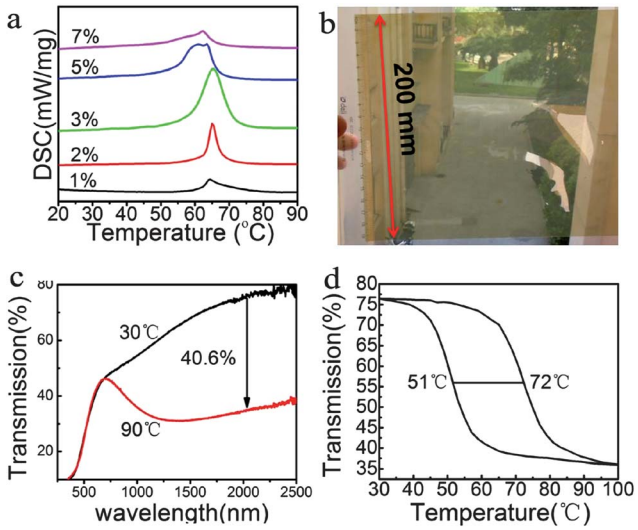

Fig. 7 (a) DSC curves of VO_2 powders with different amounts of Sb^{3+} doping; (b) an image of the film on PET *via* casting; (c) the optical transmittance spectra and (d) temperature dependence of the optical transmittance of the film at a fixed wavelength of 2000 nm.

semiconductor phase, VO_2 (M), demonstrated a monoclinic structure and two alternate V–V intervals of 2.65 Å and 3.12 Å. In this structure, the V–V pairs tilt slightly to form zigzag chains. However, the high-temperature metallic phase exhibits a tetragonal rutile structure with a regular V–V interval of 2.87 Å.[31,32] When the larger Sb^{3+} ions are substituted for the V^{4+} ions of VO_2 (M), the interval of V–V may be altered. The interval difference then becomes small, which decreases the structure difference between VO_2 (M) and VO_2 (R), and, accordingly, decreases the phase transformation activation energy. After the product became pure VO_2 (M), the doping of the Sb^{3+} ions retarded the MST phase transformation. This is probably due to the excessive substitution of Sb^{3+} ions for V^{4+} ions, which may change the structure of V–V pairing. Thus, the metal semiconductor transformation was retarded and the MST property of the VO_2 (M) was decreased with increasing Sb^{3+} doping content. The VO_2 nanoparticles with a Sb^{3+} doping content of ~3% show higher performance than pure VO_2 (M) and those with less Sb^{3+} doping contents.

Inorganic-polymer nanostructured materials have been one of the hottest topics worldwide due to the possibility of combining the physical properties of inorganic solids with the low-cost high-volume processing of plastics.[33] Colloidal VO_2 nanoparticles are fundamental materials of fast optical shutters for optical modulation and modulators in data storage and thermochromic coatings.[19–21] This work has demonstrated the advantage of the Sb^{3+}-doped VO_2 nanoparticles as a flexible energy-efficient sticking film for glass windows, which is temperature-responsive and can automatically limit the infrared transmission. Fig. 7b shows the optical photograph of the film prepared with 3%-Sb^{3+}-doped VO_2. The film is homogeneous and light brown-yellow in color. Fig. 7c and d display the corresponding optical spectra and thermochromic hysteresis of the films. In both cases, a MST transition is clearly observed to occur at about 65 °C. The film shows an integrated visible transmittance of approximately 35%. The optical properties in the infrared (IR) range are noteworthy. The IR reduction at 2000 nm across MST (40.6%; Fig. 7d) is comparable to films prepared from the common gas[34,35] and liquid phase methods (41.5%).[36]

Conclusions

In summary, this study offers a simple method for promoting the production of VO_2 (M) nanoparticles by doping. A dopant that is larger in radius and lower in valence than V^{4+} ions can introduce extra oxygen vacancies during the nucleation and growth of VO_2. This would benefit the generation of the VO_2 (M) nanoparticles with altered morphologies and minimized sizes. These nanoparticles exhibit excellent properties in MST and IR regulation, making them potential materials for application in sensor technologies and the energy-conservation fields. This synthetic strategy, which involves doping of an impurity with a different valence than the matrix cation, might be useful for controlling the solution growth of some technologically important nanomaterials.

Acknowledgements

Y.F.G. thanks the Century Program (One-Hundred-Talent Program) of the Chinese Academy of Sciences for special funding support. This study was also supported in part by a fund from the National Key Basic Research Program (NKBRP, 2009CB939904), the National Natural Science Foundation of China (NSFC, contract no: 50772126, 51172265, 51032008), Shanghai Key Basic Research Program (08JC1420300, 09DJ1400200), and high-tech project of MOST (2012AA030605, 2012BAA10B03).

References

1 D. J. Norris, A. L. Efros and S. C. Erwin, *Science*, 2008, **319**, 1776.
2 V. Mahalingam, E. Bovero, P. Munusamy, F. van Veggel, R. Wang and A. J. Steckl, *J. Mater. Chem.*, 2009, **19**, 3889.
3 F. Wang and X. G. Liu, *J. Am. Chem. Soc.*, 2008, **130**, 5642.
4 V. Mahalingam, F. Vetrone, R. Naccache, A. Speghini and J. A. Capobianco, *Adv. Mater.*, 2009, **21**, 4025.
5 F. Wang and X. Liu, *Chem. Soc. Rev.*, 2009, **38**, 976.
6 D. Chen, Y. Yu, F. Huang, P. Huang, A. Yang and Y. Wang, *J. Am. Chem. Soc.*, 2010, **132**, 9976.
7 M. N. Luwang, R. S. Ningthoujam, Jagannath, S. K. Srivastava and R. K. Vatsa, *J. Am. Chem. Soc.*, 2010, **132**, 2759.
8 C. H. Liu, H. Wang, X. R. Zhang and D. P. Chen, *J. Mater. Chem.*, 2009, **19**, 489.
9 F. Wang, Y. Han, C. S. Lim, Y. H. Lu, J. Wang, J. Xu, H. Y. Chen, C. Zhang, M. H. Hong and X. G. Liu, *Nature*, 1061, **463**.
10 S. F. Lim, W. S. Ryu and R. H. Austin, *Opt. Express*, 2010, **18**, 2309.
11 F. Zhang, G. B. Braun, Y. F. Shi, Y. C. Zhang, X. H. Sun, N. O. Reich, D. Y. Zhao and G. Stucky, *J. Am. Chem. Soc.*, 2010, **132**, 2850.
12 X. D. Feng, D. C. Sayle, Z. L. Wang, M. S. Paras, B. Santora, A. C. Sutorik, T. X. T. Sayle, Y. Yang, Y. Ding, X. D. Wang and Y. S. Her, *Science*, 2006, **312**, 1504.
13 F. Vetrone, R. Naccache, V. Mahalingam, C. G. Morgan and J. A. Capobianco, *Adv. Funct. Mater.*, 2009, **19**, 2924.
14 C. L. Jiang, F. Wang, N. Q. Wu and X. G. Liu, *Adv. Mater.*, 2008, **20**, 4826.
15 Y. F. Yang, Y. Z. Jin, H. P. He, Q. L. Wang, Y. Tu, H. M. Lu and Z. Z. Ye, *J. Am. Chem. Soc.*, 2010, **132**, 13381.
16 Y. S. Liu, D. T. Tu, H. M. Zhu, R. F. Li, W. Q. Luo and X. Y. Chen, *Adv. Mater.*, 2010, **22**, 3266.
17 L. Dai, C. Cao, Y. Gao and H. Luo, *Sol. Energy Mater. Sol. Cells*, 2011, **95**, 712–715.

18 L. T. Kang, Y. F. Gao, Z. T. Zhang, J. Du, C. X. Cao, Z. Chen and H. J. Luo, *J. Phys. Chem. C*, 2010, **114**, 1901.
19 T. D. Manning, I. P. Parkin, M. E. Pemble, D. Sheel and D. Vernardou, *Chem. Mater.*, 2004, **16**, 744.
20 C. H. Chen and Z. P. Zhou, *Appl. Phys. Lett.*, 2007, **91**, 3.
21 B. J. Kim, Y. W. Lee, B. G. Chae, S. J. Yun, S. Y. Oh, H. T. Kim and Y. S. Lim, *Appl. Phys. Lett.*, 2007, **90**, 3.
22 F. J. Morin, *Phys. Rev. Lett.*, 1959, **3**, 34.
23 G. I. Petrov, V. V. Yakovlev and J. Squier, *Appl. Phys. Lett.*, 2002, **81**, 1023.
24 C. X. Cao, Y. F. Gao and H. J. Luo, *J. Phys. Chem. C*, 2008, **112**, 18810.
25 K. C. Kam and A. K. Cheetham, *Mater. Res. Bull.*, 2006, **41**, 1015.
26 E. Strelcov, Y. Lilach and A. Kolmakov, *Nano Lett.*, 2009, **9**, 2322.
27 J. M. Baik, M. H. Kim, C. Larson, A. M. Wodtke and M. Moskovits, *J. Phys. Chem. C*, 2008, **112**, 13328.
28 J. Y. Chou, J. L. Lensch-Falk, E. R. Hemesath and L. J. Lauhon, *J. Appl. Phys.*, 2009, **105**, 6.
29 J. H. Son, J. Wei, D. Cobden, G. Z. Cao and Y. N. Xia, *Chem. Mater.*, 2010, **22**, 3043.
30 Y. Oka, S. Sato, T. Yao and N. Yamamoto, *J. Solid State Chem.*, 1998, **141**, 594.
31 J. B. Goodenough, *J. Solid State Chem.*, 1971, **3**, 490.
32 P. Jin and S. Tanemura, *Jpn. J. Appl. Phys., Part 1*, 1994, **33**, 1478.
33 Y. Yin and A. P. Alivisatos, *Nature*, 2005, **437**, 664–670.
34 M. Maaza, K. Bouziane, J. Maritz, D. S. McLachlan, R. Swanepool, J. M. Frigerio and M. Every, *Opt. Mater.*, 2000, **15**, 41.
35 R. Binions, G. Hyett, C. Piccirillo and I. P. Parkin, *J. Mater. Chem.*, 2007, **17**, 4652.
36 L. T. Kang, Y. F. Gao and H. J. Luo, *ACS Appl. Mater. Interfaces*, 2009, **1**, 2211.